RMetS Royal Meteorological Society

# Linking Northern Hemisphere temperature extremes to Rossby wave packets

G. Fragkoulidis,[a]* V. Wirth,[a] P. Bossmann[b] and A. H. Fink[b]

[a]*Institute for Atmospheric Physics, Johannes Gutenberg University, Mainz, Germany*
[b]*Institute of Meteorology and Climate Research, Karlsruhe Institute of Technology, Germany*

*Correspondence to: G. Fragkoulidis, Institute for Atmospheric Physics, Johannes Gutenberg University, Johann-Joachim-Becher-Weg 21, 55128 Mainz, Germany. E-mail: gfragkou@uni-mainz.de

**This work investigates the statistical linkage between upper-tropospheric transient Rossby wave packets (RWPs) and lower-tropospheric temperature extremes in the Northern Hemisphere during the period 1979–2015. Data from ERA-Interim reanalyses are used for the diagnosis of RWP amplitude and temperature anomalies as well as the systematic examination of their connection. Areas of large RWP amplitude are found to be associated with an increased probability of lower-tropospheric temperature extremes in many regions of the midlatitudes. Although a seasonal and inter-regional variability is apparent, this link is always stronger than in an analysis using a circumglobal waviness metric based on Fourier wavenumber amplitudes.**

**Further insight is gained by complementing the climatological results with an investigation of the two most severe recent heat waves in Europe, viz. during the 2003 and 2010 summers. Both events are found to be associated with conspicuous non-circumglobal RWPs, but differences between the two events suggest that the mechanisms linking RWPs and temperature extremes are case-dependent. The aforementioned results underscore the important role of upper-troposphere dynamics and open up avenues for future research on heat waves and cold spells at both weather and climate time-scales.**

*Key Words:* Rossby wave packets; temperature extremes; heat waves

*Received 23 August 2017; Revised 01 December 2017; Accepted 14 December 2017; Published online in Wiley Online Library 6 February 2018*

## 1. Introduction

Episodes with extreme temperatures near the Earth's surface have profound impacts on natural ecosystems, human health, and the economy (e.g. Horton *et al.*, 2016). Recent examples include the 2003 heat wave over Europe (Fink *et al.*, 2004; García-Herrera *et al.*, 2010), the 2010 heat wave over Russia (Matsueda, 2011), and the cold winter over eastern North America in 2014 (Davies, 2015). Owing to global warming, heat waves are expected to become a more serious problem in future decades (Meehl and Tebaldi, 2004; Rahmstorf and Coumou, 2011; Stocker *et al.*, 2014). For instance, an event like the 2003 European heat wave, which at that time was unprecedented in recorded history, is likely to occur every other summer by the end of the 21st century (Schär *et al.*, 2004; Russo *et al.*, 2014).

Midlatitude temperature extremes near the surface are often associated with strong Rossby wave activity in the upper troposphere (Schubert *et al.*, 2011; Lau and Nath, 2014). In particular, perturbations in the meridional flow component associated with Rossby wave activity lead to the advection of the basic-state isotherms and the consequent formation of troughs and ridges (Lackmann, 2011). This large-scale setting is conducive to physical processes which may lead to the formation of air masses with extreme temperatures (Bieli *et al.*, 2015). If, in addition, the individual troughs and ridges within the wave pattern move with a small phase velocity or are quasi-stationary, they constitute a large-scale setting where an extended episode of unusually warm or cold weather is likely to occur (Kyselý, 2008).

Investigating the linkage between near-surface temperature extremes and upper-tropospheric 'waviness' is essential for at least two reasons. Firstly, from a climate perspective, changes of temperature variability at regional scale are, to a certain extent, controlled by large-scale dynamical processes (Garfinkel and Harnik, 2017), therefore uncertainties in the future evolution of the dynamic aspects of atmospheric circulation limit the robustness of regional climate projections (Shepherd, 2014). The rapid warming near the surface in the Arctic (Arctic amplification), the enhanced warming in the tropical upper troposphere, and the cooling in the polar stratosphere are all likely to affect the variability of the midlatitude flow, but the resulting impact on weather extremes is not yet entirely clear (Butler *et al.*, 2010; Sun *et al.*, 2013; Harvey *et al.*, 2014; Barnes and Screen, 2015;

The copyright line for this article was changed on 23 February after original online publication.

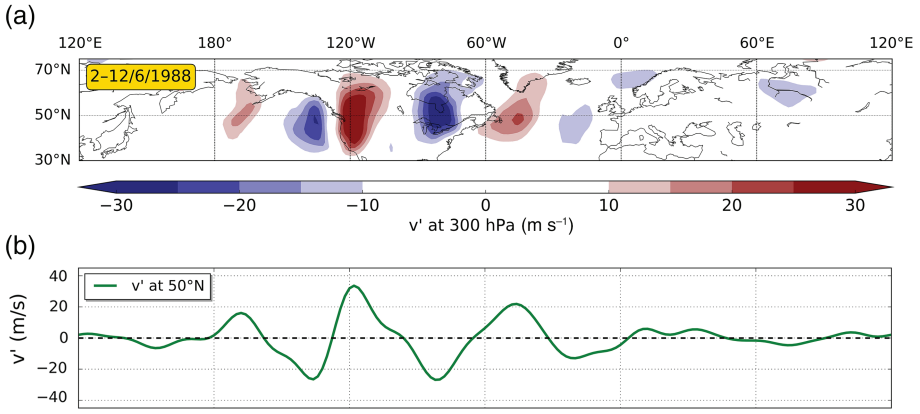


**Figure 1.** (a) Map of the 10-day mean (2–12 June 1988) meridional wind anomaly $v'$ (colour, m s$^{-1}$) at 300 hPa; (b) meridional wind anomaly $v'$ at 50°N (m s$^{-1}$).

Schneider *et al.*, 2015; Hoskins and Woollings, 2015). Secondly, from a weather forecasting perspective, it has been argued that the occurrence of long-lived Rossby wave packets (RWPs) can lead to enhanced predictability in certain situations (Lee and Held, 1993; Grazzini and Vitart, 2015). Associated with that, it has long been known that smaller-scale weather features may inherit predictability from larger-scale dynamical features (Anthes *et al.*, 1985). Therefore, it is highly desirable to have a sound understanding of the strength of the linkage between upper-tropospheric waviness and lower-tropospheric temperature extremes, along with its inter-regional and seasonal variability.

The present article aims to further our understanding of these aspects. Since upper-tropospheric Rossby waves tend to organize in spatially confined and possibly coherent wave packets (Chang, 1993), we propose a novel perspective that focuses on RWPs rather than circumglobal Rossby waves (e.g. Screen and Simmonds, 2014). A RWP is said to exist whenever the amplitude of a Rossby wave varies with longitude such that it reaches a maximum over a certain longitude with a gradual decay both westward and eastward (Chang, 2001). Such structures are found in both observations and in a hierarchy of models (Lee and Held, 1993). Coherent RWPs propagate eastward with the so-called group velocity, while the embedded eddies propagate with their individual phase velocities, which are typically smaller than the group velocity (Chang, 1993; Esler and Haynes, 1999). In recent studies, it is increasingly recognized that RWPs play an important role in various contexts relevant for both weather and climate (Martius *et al.*, 2008; Wirth and Eichhorn, 2014; Souders *et al.*, 2014; Quinting and Jones, 2016; Teubler and Riemer, 2016).

Figure 1 gives an example from June 1988, when the western part of the Northern Hemisphere was characterized by a large-amplitude RWP, while the flow was close to zonal in the eastern part of the Northern Hemisphere. This RWP was associated with a pronounced heat wave over the Midwest of the USA (Lyon and Dole, 1995; Schubert *et al.*, 2011), which was mediated by a quasi-stationary ridge over that region. It is well known that persistent ridging over a region during summer facilitates the formation of a heat wave, and Figure 1 shows that, even in a 10-day running mean (which tends to produce smooth hemispheric-wide wave patterns), this does not require the Rossby wave to be of circumglobal nature by necessity (also Röthlisberger *et al.*, 2016). Nevertheless, this is worth pointing out and investigating further, in view of recent studies connecting the occurrence of some major heat waves to large-amplitude circumglobal waves as quantified by Fourier wavenumber amplitudes (Petoukhov *et al.*, 2013; Kornhuber *et al.*, 2017).

In this article we suggest that the local amplitude of propagating RWPs is a more appropriate metric of the upper-tropospheric waviness in the present context than the Fourier amplitudes of circumglobal waves. We will quantify the statistical connection between RWP amplitudes and lower-tropospheric temperature extremes and show that this is indeed an improvement over the use of Fourier amplitudes. In addition, we will compute the spatial distribution of this statistical linkage over the entire Northern Hemisphere for both the summer and winter seasons. Finally, we complement our statistical analysis with case-studies of two prominent recent heat waves (2003 in western Europe and 2010 in Russia) in terms of their associated RWP signatures. These studies will seek an illustration of the case-to-case variability (within the sample used in our statistical analysis) in aspects of the temperature extremes and the corresponding role of RWPs.

The article is organized as follows. First, the data used, the calculation of anomaly fields, the diagnosis of RWPs, and a heat wave index are introduced in section 2. Thereafter, results regarding the statistical linkage between upper-tropospheric waviness (RWP amplitude) and lower-tropospheric temperature extremes are presented in section 3. This analysis is complemented in section 4 with an investigation of the role of RWPs during the 2003 and 2010 heat waves. Finally, a summary of our main results and some discussion are provided in section 5.

## 2. Data and methods

### 2.1. *Reanalysis data*

Our investigation is based on data from the ERA-Interim reanalysis project (Dee *et al.*, 2011) at the European Centre for Medium-Range Weather Forecasts (ECMWF). We used the meridional wind $v$ at 300 hPa, geopotential $\Phi$ at 300 hPa, and temperature $T$ at both 850 hPa and 2 m. Note that the 2 m temperature field analysis in ECMWF is performed using a relatively simple data interpolation scheme following the upper-air atmospheric four-dimensional variational analysis. We retrieved the data on a $2^\circ \times 2^\circ$ horizontal resolution with a temporal resolution of 6 h (daily at 0000, 0600, 1200 and 1800 UTC), spanning the period from January 1979 to December 2015. Unless stated otherwise, daily means obtained by averaging the four values within each day are used. In cases where an averaging over a limited region was applied, the mean over the respective grid points was computed with a weighting by the cosine of latitude, in order to be consistent with a true area average.

### 2.2. *Computation of anomalies*

Here we are primarily concerned with synoptic-scale transient features. Therefore, we defined 6-hourly anomalies (denoted by a prime) as deviations from climatology as follows:

$$\psi'(\lambda,\phi,t) = \psi(\lambda,\phi,t) - \overline{\psi}(\lambda,\phi,t_\mathrm{d}) - \psi_l(\lambda,\phi,t). \qquad (1)$$

Here, $\psi$ represents any of the variables $v$, $\Phi$, or $T$, $\lambda$ denotes longitude, $\phi$ denotes latitude, $t$ denotes time, and $t_\mathrm{d}$ denotes a particular timestep within the climatological year (e.g. 1800 UTC on 5 February). In the above equation, $\overline{\psi}(\lambda,\phi,t_\mathrm{d})$ represents the climatology at $t_\mathrm{d}$; it was obtained by first averaging the 37 values

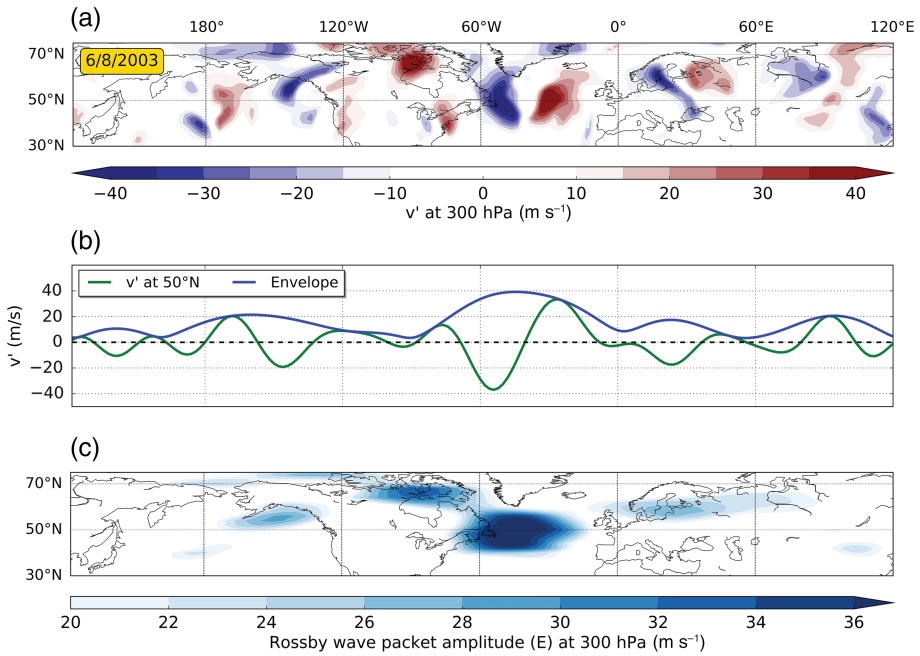


**Figure 2.** RWP diagnosis example for 6 August 2003 0000 UTC. (a) Map of the meridional wind anomaly $v'$ (colour, m s$^{-1}$) at 300 hPa; (b) meridional wind anomaly $v'$ at 50°N (green line, m s$^{-1}$) and its envelope $E$ (blue line, m s$^{-1}$); (c) map of the envelope field $E$ (RWP amplitude, m s$^{-1}$).

of the variable for each $t_d$ over the 37 years available (1979–2015). By design, the resulting function is periodic in time (with a period of one year), but it shows strong noise owing to the relatively small number of years to be averaged over. We, therefore, performed a Fourier series expansion and discarded the higher harmonics, keeping only the lowest four frequencies (1 to 4 year$^{-1}$). In addition, we detrended the anomalies by subtracting the 1979–2015 linear regression $\psi_l(\lambda, \phi, t)$ of the variable at each grid point.

### 2.3. *Diagnosing Rossby wave packets*

The diagnosis of upper-tropospheric RWPs was performed using the meridional wind anomaly $v'(\lambda, \phi, t)$ at 300 hPa (Figure 2(a)). In particular, we computed the envelope $E(\lambda, \phi, t)$ of $v'(\lambda, \phi, t)$ following the ideas of Zimin *et al.* (2003). The envelope field is non-negative everywhere and can be taken as a measure of RWP amplitude. By design, it eliminates the phase of the carrier wave (i.e. the location of troughs and ridges) and thus allows one to focus on the RWP as a whole. We modified the algorithm of Zimin *et al.* (2003) by implementing a number of refinements. For instance, we filtered the fields by multiplying the Fourier coefficients with an adjustable Tukey window (cosine lobe convolved with a rectangle window; Harris, 1978) instead of a boxcar window; this allows us to achieve a smoother transition between latitudes. In addition, following the approach of Wolf and Wirth (2015), we computed the envelope in semi-geostrophic coordinate space. This is motivated by the desire to reduce spurious fragmentation of RWPs, which arises from the semi-geostrophic nature of Rossby waves in combination with the method of Zimin *et al.* (2003). In summary, we performed the following steps:

(i) For each latitude, we filtered the fields of $v'$ and $\Phi'$ in the zonal direction, keeping wavelengths roughly between $\lambda_1 = 2000$ km and $\lambda_2 = 10\,000$ km. This is done by multiplying the Fourier coefficients with a Tukey window. First we calculated the (non-integer) zonal wavenumber limits $s_1$ and $s_2$ corresponding to $\lambda_1$ and $\lambda_2$, respectively. The non-zero part of the Tukey window then spans the total zonal wavenumber range $[s_2 - 1.5, s_1 + 1.5]$, with its cosine-tapered parts accounting for 30% of the total window range.
(ii) We applied a semi-geostrophic coordinate transformation as described in Wolf and Wirth (2015) using the filtered $\Phi'$.
(iii) The transformed $v'$ field in the new coordinate system was linearly interpolated back to a regular (latitude–longitude) grid and was filtered again, as in step (i).
(iv) Lastly, the envelope $E$ was computed from $v'$ separately for each latitude with the so-called Hilbert transform method (Zimin *et al.*, 2003) without applying any additional filter (Figure 2(b)).

Repeating these steps for every latitude resulted in the two-dimensional $E(\lambda, \phi, t)$ field (Figure 2(c)).

### 2.4. *Heat wave index*

We used a modified version of the heat wave magnitude index daily (HWMId) by Russo *et al.* (2015) to detect regions that are affected by abnormally high surface temperatures. This index measures the 'extremeness' of the daily maximum 2 m temperature $T_{dm}$ at each grid point compared to climatology. In this study, the climatology was obtained from the ERA-Interim data. The HWMId was computed as the sum of the 'daily magnitude' $M_d$ of all days from the considered heat wave episode; the daily magnitude $M_d$, in turn, was defined as

$$M_d(T_{dm}) = \begin{cases} \dfrac{T_{dm} - T_{25p}}{T_{75p} - T_{25p}} & \text{if } T_{dm} > T_{25p}, \\ 0 & \text{if } T_{dm} \leq T_{25p}, \end{cases} \qquad (2)$$

where $T_{25p}$ and $T_{75p}$ denote the 25th and the 75th percentile, respectively, of the climatological distribution of $T_{dm}$, and $T_{75p} - T_{25p}$ is the corresponding interquartile range. Because of its reference to local climatology, the HWMId allows one to compare heat wave periods in different climatic regions in a meaningful way. In contrast to Russo *et al.* (2015), here the climatological distribution of $T_{dm}$ was estimated from the reference period 1979–2015 using the $31 \times 37 = 1147$ values of $T_{dm}$ which correspond to the 31-day window centred on the respective day of each year (thus achieving a smooth day-to-day variation of $T_{25p}$ and $T_{75p}$). This way, it takes into account the annual cycle in 2 m temperature and the heat wave identification is not biased toward summer, allowing one to study anomalously hot events year-round. In summary, the HWMId combines a measure of the deviation from climatology with a measure of the length of the episode.

## 3. Connection between upper-tropospheric waviness and lower-tropospheric temperature anomalies

### 3.1. Analysis for a European region in summer

Firstly, as an example, the connection between RWP amplitudes at 300 hPa and temperature anomalies at 850 hPa is quantified for the Northern Hemisphere summer (June, July, and August; JJA) in a region of Europe. In the following subsection it will be extended to the entire Northern Hemisphere Extratropics for both the summer and winter seasons. All results presented in this and the following section are reasonably robust in the sense that small changes in user-defined parameters do not lead to qualitative changes in the results. Details about related sensitivity tests can be found in Appendix A.

A temperature is considered to be anomalous to the extent that its daily anomaly $T'$ deviates from climatology in either direction (warm or cold). In other words, we consider daily mean $|T'|$ at 850 hPa as our metric for anomalous temperature. The daily mean RWP amplitude at 300 hPa is quantified through the daily mean envelope $E$, as described in section 2. We focus our attention on synoptic-scale temperature extremes, therefore both $|T'|$ and $E$ are averaged over an area covering parts of southern and central Europe, viz. 36–56°N and 0–20°E . We draw on the data from all available summers (1979–2015), but we use only every third day in a consecutive sequence of summer days in order to minimize the impact of serial correlation on the results, without strongly decreasing our sample size.

Figure 3(a) shows the result in the form of a scatter plot. The two time series have been normalized by subtracting their means and dividing by their standard deviations. This facilitates the comparison with the Fourier amplitude analysis discussed below. Evidently, there is an increase of $|T'|$ with RWP amplitude and the Spearman's rank correlation coefficient of $\rho = 0.44$ suggests a moderately strong yet significant ($p$-value well below 0.001) connection between the two fields. The data points are then divided into ten equally populated bins, indicated by the dashed vertical lines, which will be referred to as $E$-bins below. The 90th percentile of the $|T'|$ distribution is indicated by the horizontal blue line. In the following, we are going to refer to a temperature anomaly as 'extreme' if it exceeds the 90th percentile, i.e. if the data point on the scatter diagram lies above the blue line.

Focusing on the temperature extremes, Figure 3(a) shows that the fraction of points above the blue line is significantly larger for the rightmost $E$-bin than for the lower-lying $E$-bins. This means that the probability for a temperature extreme is significantly larger on days with a strong RWP amplitude than on other days with weaker RWP amplitudes. To quantify this connection, we plot in Figure 3(b) the percentage $P_{\mathrm{ex}}(E)$ of days with extreme temperatures for each $E$-bin. $P_{\mathrm{ex}}(E)$ can be interpreted as the probability of a temperature extreme for a given value of the RWP amplitude. The red shading indicates the statistical uncertainty ($\Delta P_{\mathrm{ex}}$), which we estimated as

$$\Delta P_{\mathrm{ex}}(E) = \Delta\left(\frac{n_{\mathrm{ex}}(E)}{n(E)}\right) = \frac{\Delta n_{\mathrm{ex}}(E)}{n(E)} = \frac{\sqrt{n_{\mathrm{ex}}(E)}}{n(E)}, \qquad (3)$$

where $n(E)$ is the total number of points in the $E$-bin and $n_{\mathrm{ex}}(E)$ is the corresponding number of extreme temperatures in this bin. Given this sampling, there is a near-exponential increase of $P_{\mathrm{ex}}(E)$ with RWP amplitude for the considered region in Europe. On a day with a very large RWP amplitude (above the 90th percentile of the RWP amplitude distribution), the probability for a warm/cold temperature extreme is approximately 40%. Furthermore, since each bin is one tenth of the sample size and temperature extremes also constitute 10% of it, this result can be interpreted in an equivalent way by saying that approximately 40% of all the temperature extremes occur in the highest $E$-bin (corresponding to the 90th percentile).

As mentioned in the introduction, there has been a number of earlier investigations on the connection between temperature extremes and atmospheric dynamics, and some of these studies used Fourier amplitudes to quantify the waviness of the upper-tropospheric flow in this regard. Therefore, we will now address the question of how appropriate Fourier amplitudes are in quantifying the connection between an individual temperature extreme and upper-tropospheric waviness. For this purpose we repeated the above analysis, but we replaced the RWP amplitude over the region in Europe by the normalized root mean square of the Fourier transform zonal wavenumber 1–15 amplitudes of the 300 hPa $v'$, meridionally averaged over 36–56°N . Figures 3(c) and (d) show the corresponding scatter plot and quantile analysis in a format similar to Figures 3(a) and (b), respectively. Apparently, the correlation in Figure 3(c) is much less pronounced than in Figure 3(a), with a much lower value $\rho = 0.19$ (instead of 0.44) of the Spearman's correlation coefficient (again, the value of $\rho$ is statistically significant against the null hypothesis of no correlation). As a result, the increase of $P_{\mathrm{ex}}$ with Fourier amplitude in Figure 3(d) is much weaker than the corresponding behaviour in Figure 3(b). This is due to cases where a temperature extreme is associated with high waviness confined over Europe and relatively weak Fourier amplitudes.

In the null-case of no statistical connection between upper-tropospheric waviness and temperature extremes, each point in Figures 3(b) and (d) would be associated with roughly the same fraction of temperature extremes, i.e. 10% plus/minus statistical fluctuations, and the function $P_{\mathrm{ex}}$ would be more or less flat. To the extent that there is a non-trivial statistical connection, one expects the function values on the ordinate to increase with increasing values on the abscissa. Motivated by this, we quantify the strength of the statistical connection between upper-tropospheric waviness and 850 hPa temperature extremes by computing the fraction $F$ between the value in the highest and the lowest bin in Figures 3(b) and (d), respectively. We obtain $F = 39.5/1.8 \approx 21.9$ for the analysis with RWP amplitudes, but only $F = 17.5/6.2 \approx 2.8$ for the analysis with Fourier amplitudes. Both results are statistically significant (the former even highly significant), as can be gleaned from the size of the uncertainty band (red) in relation to the difference between the respective values in the top and bottom bin. These results indicate that the RWP amplitudes are *much* more appropriate than Fourier amplitudes to quantify the connection between individual temperature extremes and upper-tropospheric waviness.

### 3.2. Extension to the entire Northern Hemisphere Extratropics

It is not clear at this point to what extent the results of the analysis in Figure 3 carry over to other regions and seasons of the Northern Hemisphere. For reference, Appendix B provides Northern Hemisphere summer and winter regional climatologies for the 90th percentile of $|T'|$ at 850 hPa, $|T'|$ at 2 m, RWP amplitude ($E$), and the root mean square of the Fourier transform zonal wavenumber 1–15 amplitudes of the 300 hPa $v'$ (Figure B1). The inter-regional and seasonal variability of the aforementioned fields facilitate the interpretation of the hemispheric analyses which follow.

We repeat the correlation analysis from the previous subsection for individual $20^\circ \times 20^\circ$ regions centred on every grid point in the Northern Hemisphere Extratropics for both summer (JJA) and winter (DJF). In order to compress information, we keep for each grid point only the percentage $P_{\mathrm{ex}}$ of days with extreme temperature that occur in the top 20% of RWP or Fourier amplitudes, respectively. In other words, we use

$$\mathcal{P} = P_{\mathrm{ex}}(\text{top 20\% RWP or Fourier amplitudes}) \qquad (4)$$

as a measure for the connection between 850 hPa temperature extremes and 300 hPa waviness. The result for the summer season is shown in Figure 4(a). In many areas of the Northern Hemisphere, $\mathcal{P} > 50\%$, meaning that there is a greater than 50% probability of a temperature extreme occurrence on a day with

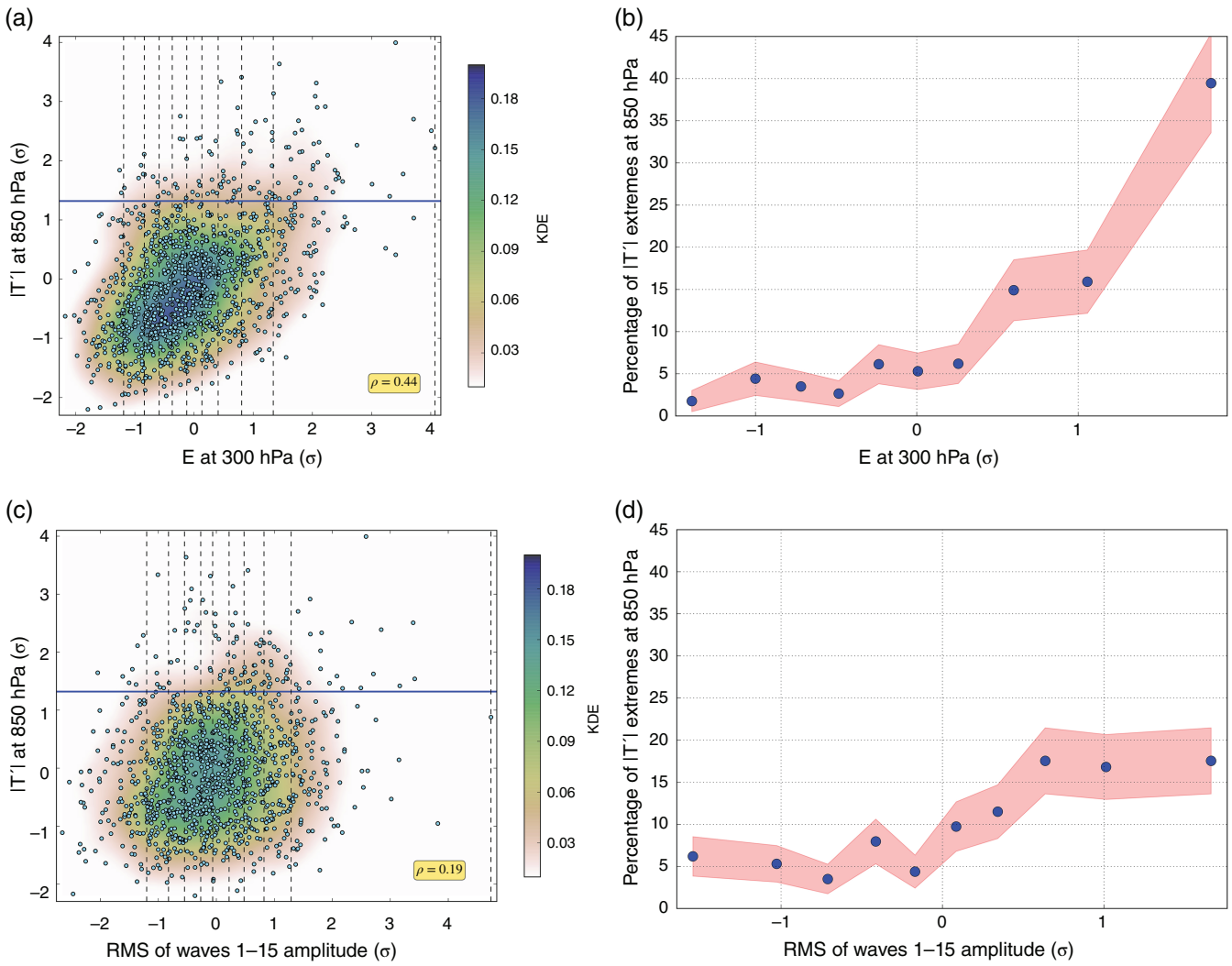


**Figure 3.** Analysis of the temporal correlation between daily mean RWP amplitudes at 300 hPa and temperature anomalies at 850 hPa for the 36–56°N , 0–20°E region in Europe during JJA. (a) Scatter plot of normalized $|T'|$ against normalized $E$. The colour shading depicts a kernel-density estimate using Gaussian kernels. The vertical dashed lines indicate specific quantiles of the values for $E$ separating the data into ten equally populated bins. The horizontal blue line depicts the 90th percentile of the temperature distribution. The Spearman's rank correlation coefficient is shown in the yellow box. (b) Percentage (%) of temperature extremes (daily average $|T'| >$ 90th percentile) in each $E$-bin, where each $E$-bin is represented on the abscissa by its median. The red shading shows the statistical uncertainty $\Delta P_{ex}(E)$ of each value. (c), (d) are as (a) and (b), except that the horizontal axis now refers to the normalized Fourier amplitude instead of RWP amplitude (see text for explanation).

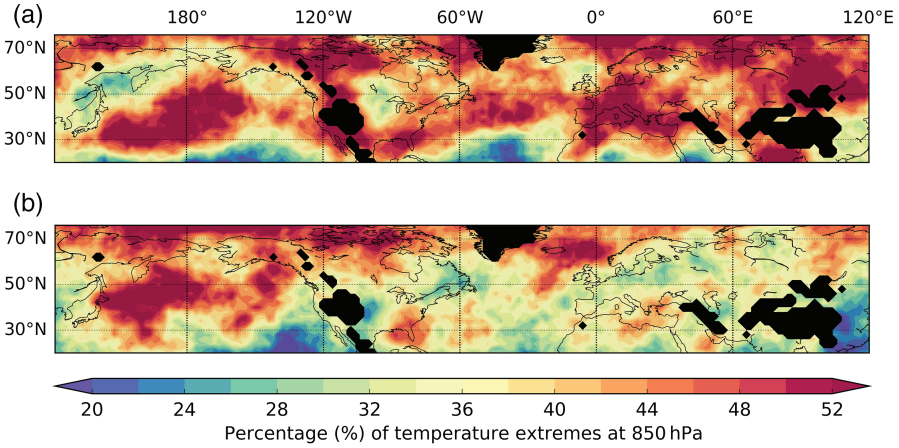


**Figure 4.** Percentage $\mathcal{P}$ of temperature extremes at 850 hPa for (a) JJA and (b) DJF days with strong upper-tropospheric waviness, as measured by RWP amplitudes. The value for each grid point corresponds to the 20° ×20° region which is centred on it. Grid points with a mean surface pressure below 850 hPa are shown in black.

a strong RWP amplitude (above the 80th percentile). The areas of highest $\mathcal{P}$ include most of Europe, Central Asia, and parts of North America and the North Pacific. Notable minima occur north of the UK, in Central North America, and in the Sea of Okhotsk. The corresponding plot for the winter season is shown in Figure 4(b). In this case the connection between $E$ and $|T'|$ is not as strong as in summer. Inherent differences in the dynamic and thermodynamic characteristics of the two seasons account for the different $\mathcal{P}$ distributions. Some discussion on the issue is given in section 5.

The connection with Fourier amplitude is again much weaker than the connection with RWP amplitude, and similarly the values of $\mathcal{P}$ in winter are lower than those in summer (Figures 5(a) and (b)). This result corroborates that, throughout the Northern

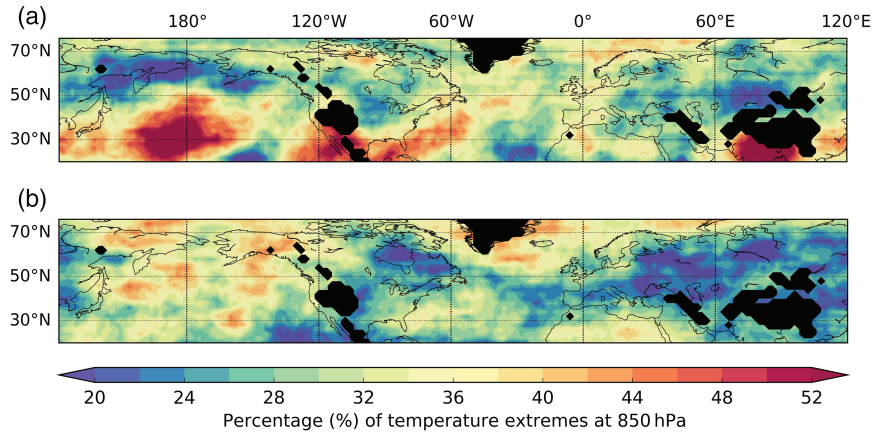


**Figure 5.** Percentage $\mathcal{P}$ of temperature extremes at 850 hPa for (a) JJA and (b) DJF days with strong upper-tropospheric waviness, as measured by Fourier amplitudes. For each grid point, $|T'|$ is averaged over the $20^\circ \times 20^\circ$ region which is centred on it and the corresponding Fourier amplitudes are calculated from the 300 hPa $v'$ field, meridionally averaged over the $20^\circ$ zonal band that covers the latitudinal extent of the respective region. Grid points with a mean surface pressure below 850 hPa are shown in black.

Hemisphere, Fourier amplitudes are less appropriate than RWP amplitudes to quantify the link between upper-tropospheric waviness and individual temperature extremes; and in most regions the difference between the two methods is substantial. The reason for this result is fairly straightforward: an individual temperature extreme of synoptic scale does not require a circumglobal Rossby wave; rather, a more localized wave packet is sufficient. Of course, even a localized RWP can be decomposed in a Fourier series, but the resulting Fourier amplitudes are smaller than for a circumglobal Rossby wave of similar amplitude. In this regard, a 'sharper' diagnostic of upper-tropospheric waviness like the RWP amplitude provides essential inter-regional information when studying the climatological linkage to lower-tropospheric temperature extremes.

### 3.3. *Near-surface temperature anomalies*

So far, a clear link between upper-tropospheric RWP amplitude and 850 hPa temperature extremes has been found. However, this does not necessarily imply a similar link with near-surface temperature extremes. Various boundary-layer processes (associated with e.g. topography, low clouds, soil moisture) can have an impact on the strength of this link, and these processes may vary with location and time. Figure 6 shows the connection between RWP amplitude and 2 m temperature extremes. As expected, during both summer and winter, the values of $\mathcal{P}$ are lower than for the corresponding analysis with 850 hPa temperature. However, during summer there are still several areas in the Northern Hemisphere with $\mathcal{P} > 40\%$ (e.g. most of Europe, Central Asia and western North America). Taking the 2 m temperature extremes, we obtain $F = 26.3/4.4 \approx 6.0$ over the European region considered in section 3.1. This is still much larger than 1, but considerably lower than for the corresponding analysis with 850 hPa temperature extremes (section 3.1).

The above result implies that the correlation between 850 hPa and 2 m temperature anomalies must be subject to substantial inter-regional and seasonal variability. For illustration we consider first two European sites, Madrid and London, during summer. For this analysis, the arithmetic mean of the 1200 and 1800 UTC temperature anomalies (in the $2^\circ \times 2^\circ$ grid points that correspond to these sites) is used instead of daily mean temperature anomaly. Figure 7 shows the scatter plot of 2 m temperature (abscissa) versus the corresponding 850 hPa temperature (ordinate). The temperature values are expressed in percentiles of their distribution in order to facilitate the comparison between different locations.

The Madrid area shows a good correlation between the temperatures at both levels, with a rather pronounced symmetry about the diagonal ($x = y$ axis). The correlation is particularly good at the extreme ends of the distribution, i.e. for pronounced temperature anomalies. In contrast, the correlation for the London area is much weaker, showing a strong scatter of the points at the extreme ends of the distribution and a pronounced asymmetry about the diagonal. For example, while strong warm anomalies at 2 m in London almost always coincide with a strong warm anomaly at 850 hPa, the reverse is not true, i.e. strong warm anomalies at 850 hPa are not necessarily associated with strong warm anomalies at 2 m. Distinct topography and boundary-layer properties in these two sites account to some extent for these differences.

The link between 850 hPa and 2 m temperature extremes is now systematically analyzed for the entire Northern Hemisphere. The question we want to address is what percentage of the 850 hPa temperature extremes ($|T'_{850}| >$ 90th percentile) coincides with 2 m temperature extremes ($|T'_{2m}| >$ 90th percentile). For this analysis we again use daily mean temperatures for each grid point at both levels in order to be consistent with the temporal resolution used in the previous subsections. We divide the number of simultaneous occurrences of temperature extremes at both levels by the number of 850 hPa temperature extremes. The resulting fraction $C_2^{850}$ for JJA (Figure 8(a)) shows a large inter-regional variability, with the oceans generally featuring a much weaker linkage than the continents. This is presumably due to the fact that the 2 m temperature field over the ocean surface is more strongly influenced by the sea surface temperature (SST) than by the atmospheric temperature at 850 hPa. On the other hand, the continents show values as high as $C_2^{850} \approx 60$–$70\%$. Maxima occur in mountainous regions, which is likely due to the proximity of the 850 hPa and 2 m levels (areas with a mean surface pressure below 850 hPa are masked out).

The corresponding analysis for the winter season is shown in Figure 8(b). The inter-regional variability pattern is strikingly different from the summer season. For instance, in contrast to the summer season, winter is characterized by a non-negligible connection between the two levels over the oceans, especially in the storm track regions. Here, the strong lower-tropospheric winds and temperature gradients suppress the impact of the SST on the oceanic 2 m temperatures. On the other hand, the connection between the two levels over the continents is generally lower than in summer, presumably related to the occurrence of low-level inversions (also discussion in section 5).

## 4. The heat waves of 2003 and 2010

We now proceed from a statistical to a case-based analysis and investigate two prominent synoptic-scale temperature extremes, viz. the 2003 western European heat wave and the 2010 Russian heat wave. These two events have been studied quite extensively from a subseasonal-to-seasonal and climate perspective (e.g. Meehl and Tebaldi, 2004; Fischer *et al.*, 2007a; Otto *et al.*,

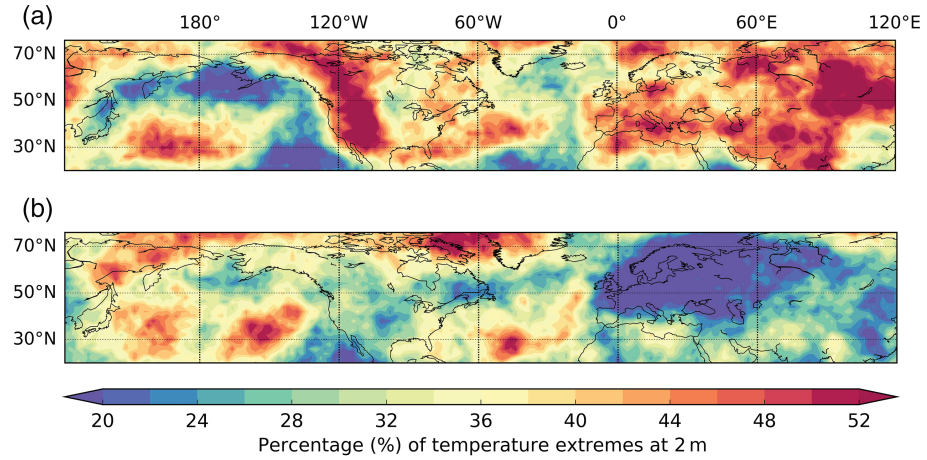


**Figure 6.** Percentage $\mathcal{P}$ of temperature extremes at 2 m for days with strong RWP amplitude for (a) JJA and (b) DJF during 1979–2015. The value for each grid point corresponds to the 20° × 20° region centred on it.

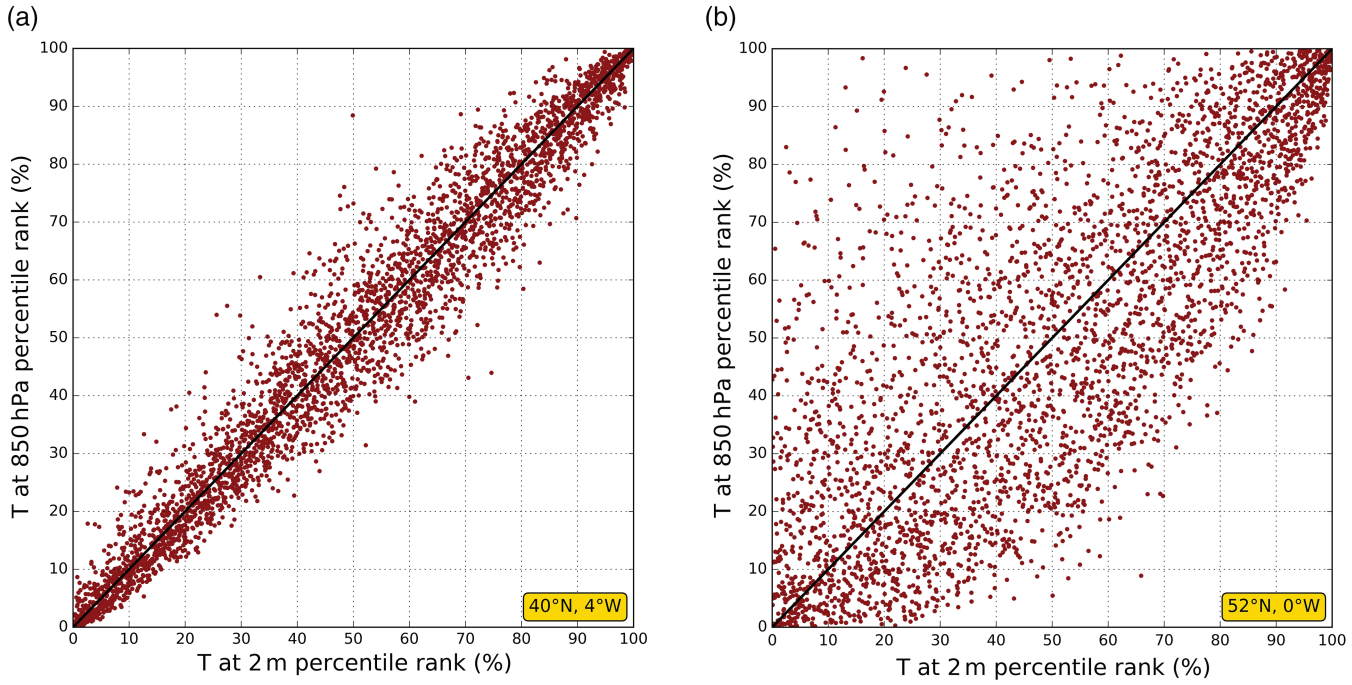


**Figure 7.** Comparison between temperature anomalies at 850 hPa and 2 m using the 1200 and 1800 UTC average values at two European sites: (a) 40°N , 4°W (Madrid) and (b) 52°N , 0°E (London). The plot contains data for all Northern Hemisphere summer days between 1979 and 2015. The temperature values are expressed in percentiles of the corresponding distribution. The black diagonal depicts the $x = y$ axis.

2012; Petoukhov *et al.*, 2013; Hauser *et al.*, 2016), whereas fewer studies have focused on the daily evolution of synoptic weather systems (Black *et al.*, 2004; Fink *et al.*, 2004; Schneidereit *et al.*, 2012). Since both of the affected regions are associated with high values of $\mathcal{P}$ (Figure 4(a)), it appears constructive to inspect the day-to-day linkage between upper-tropospheric waviness and lower-troposphere temperature anomalies over these regions during the two heat waves. In this regard, focusing on the role of upper-tropospheric RWPs will provoke novel considerations about the two events and will also contribute to our objective by emphasizing the advantages of diagnosing waviness locally.

To set the stage, we show in Figure 9 the HWMId (section 2.4) for a representative 11-day period during each of these events. In both episodes, the index shows strong deviations from climatology in an extended area. As an indication, areas with an HWMId value of 20 experienced a positive daily maximum 2 m temperature ($T_{\mathrm{dm}}$) deviation from the 25th percentile ($T_{25p}$) which was on average twice the climatological interquartile range ($T_{75p} - T_{25p}$) for 11 days. In the 2003 case, the largest 11-day HWMId accumulations are found over France, but many more parts of western Europe were also severely affected. (Since the index is based on 2 m temperature, the maximum over the North Atlantic carries an imprint of anomalously warm SSTs.) During the 2010 event, mainly western Russia and parts of Ukraine and Belarus were the affected regions.

Hovmöller diagrams have traditionally been used to reduce the complexity of the four-dimensional evolution of RWPs by representing aspects of their propagation in longitude–time coordinates (Glatt *et al.*, 2011). In Figure 10, 850 hPa temperature anomaly and RWP amplitude during the two heat waves are superimposed on Hovmöller diagrams which span the same period of the two summers. The temperature anomalies have been averaged over a 20° latitude band that roughly covers the affected areas during the respective heat wave (Figure 9). For the latitudinal averaging of RWP amplitude $E$, it proved beneficial to use a more sophisticated algorithm, since not all RWPs propagate on the same latitude bands and each of them does not necessarily follow a purely zonal track (e.g. Figure 11). First, the latitudinal interval used for the temperature anomalies was extended both northwards and southwards by 10° , resulting in an averaging interval of 40° . Within this interval we only averaged over those 20° where the highest values of $E$ occurred in a given day. This implies effectively an average over 20° in latitude as in the case of temperature anomaly, but the averaging

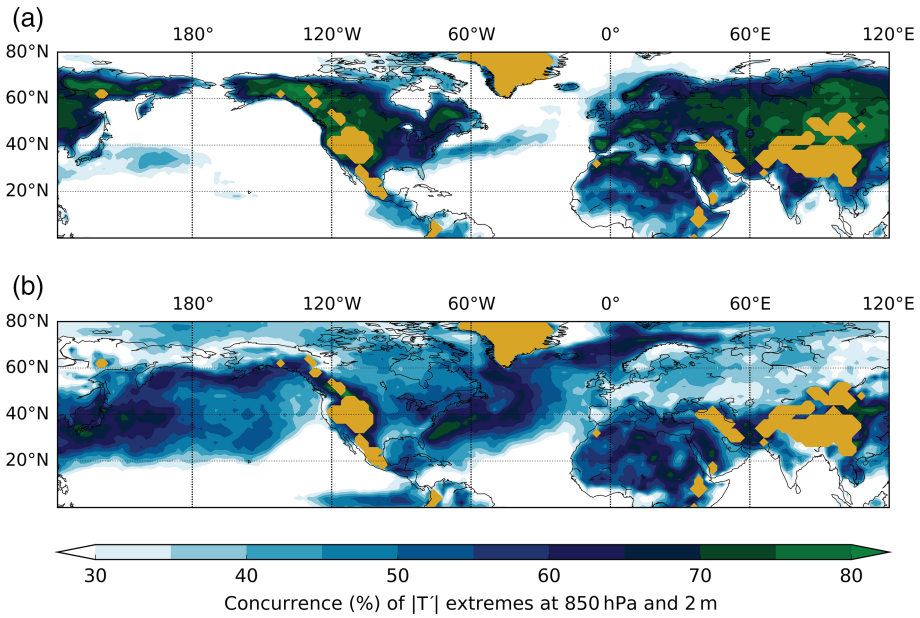


**Figure 8.** Concurrence $C_2^{850}$ (%) between 850 hPa and 2 m temperature extremes for (a) JJA and (b) DJF during 1979–2015. Grid points with a mean surface pressure below 850 hPa are shown in orange.

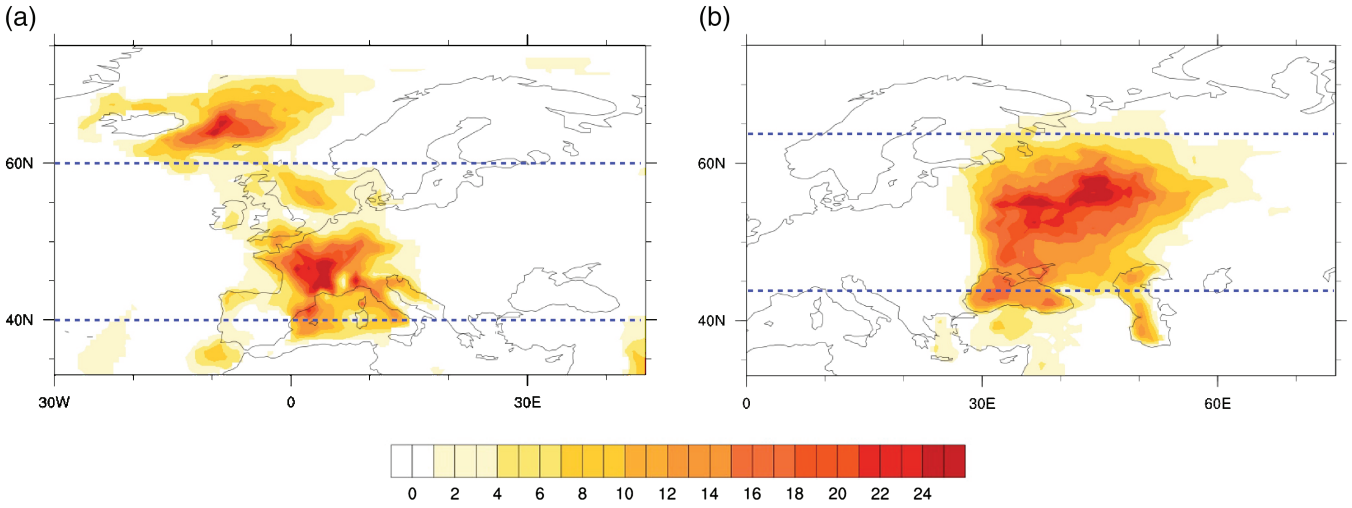


**Figure 9.** HWMId (dimensionless) for (a) 4–14 August 2003 and (b) 2–12 August 2010. The blue dashed lines indicate the latitude band of 850 hPa temperature anomaly averaging in Figure 10.

latitude range self-adjusts, such that it automatically follows the RWP location as quantified through *E*. Applying this algorithm will also be advantageous in cases of a split RWP (high waviness in distinct latitude bands of the same longitude). Finally, a weak bivariate interpolation (using cubic Hermite splines) is applied to slightly smooth the resulting RWP contours.

The first aspect to note in Figure 10 is that for both events the upper-tropospheric waviness was restricted to a part of the hemisphere. This nicely illustrates our point, that RWPs are more relevant than circumglobal Rossby waves in connection with temperature extremes. The situation is quite similar to the longitudinally confined RWP during the 1988 heat wave (Figure 1). In addition, although the heat waves of 2003 and 2010 were of similar intensity, Figure 10 shows that the 2003 event was much shorter-lived (∼ 2 weeks) than the 2010 event (∼ 5 weeks).

After an anomalously hot June (not shown here), July 2003 was characterized by slightly above normal temperatures over Europe (Fink *et al.*, 2004). This was coincident with relatively minor RWP activity over the North Atlantic and Europe, except during a short episode on 11–15 July (Figure 10(a)). In contrast, the first half of August was characterized by an anomalously strong and long-lasting RWP which formed at around 110°W and vanished in mid-August at around 70°E. This RWP acquired its maximum amplitude over the North Atlantic and Europe on 7–9 August, coincident with the hottest days over western Europe. Figure 11 illustrates in more detail the progression of this RWP, as represented by areas of very strong (35 m s$^{-1}$) RWP amplitude. During this period, it slowly propagated eastward from Newfoundland (5 August) and reached its highest intensity and extent over Northern Europe on 9 August. Thereafter it started to weaken gradually.

The key question now is how the RWP shown in Figures 10(a) and 11 contributed to the heat wave. A partial answer can be obtained through analysis of the upper-tropospheric meridional wind anomaly $v'$ in Figure 12(a). For consistency, in each time–longitude point of the Hovmöller diagram, $v'$ (colour fill) is averaged over the same latitudes as *E*. Apparently, the succession of northerly and southerly anomalies in the meridional component of the wind field, which constitute the RWP, propagate only very slowly in the zonal direction (≈3° longitude per day). This contrasts with the propagation velocity of the entire RWP, which corresponds to a group velocity of ≈15° longitude per day (green arrow in Figure 12(a)). The underlying phenomenon has long been known as 'downstream development' (Simmons and Hoskins, 1979), and indicates the transfer of wave energy toward a developing disturbance downstream (Chang, 1993).

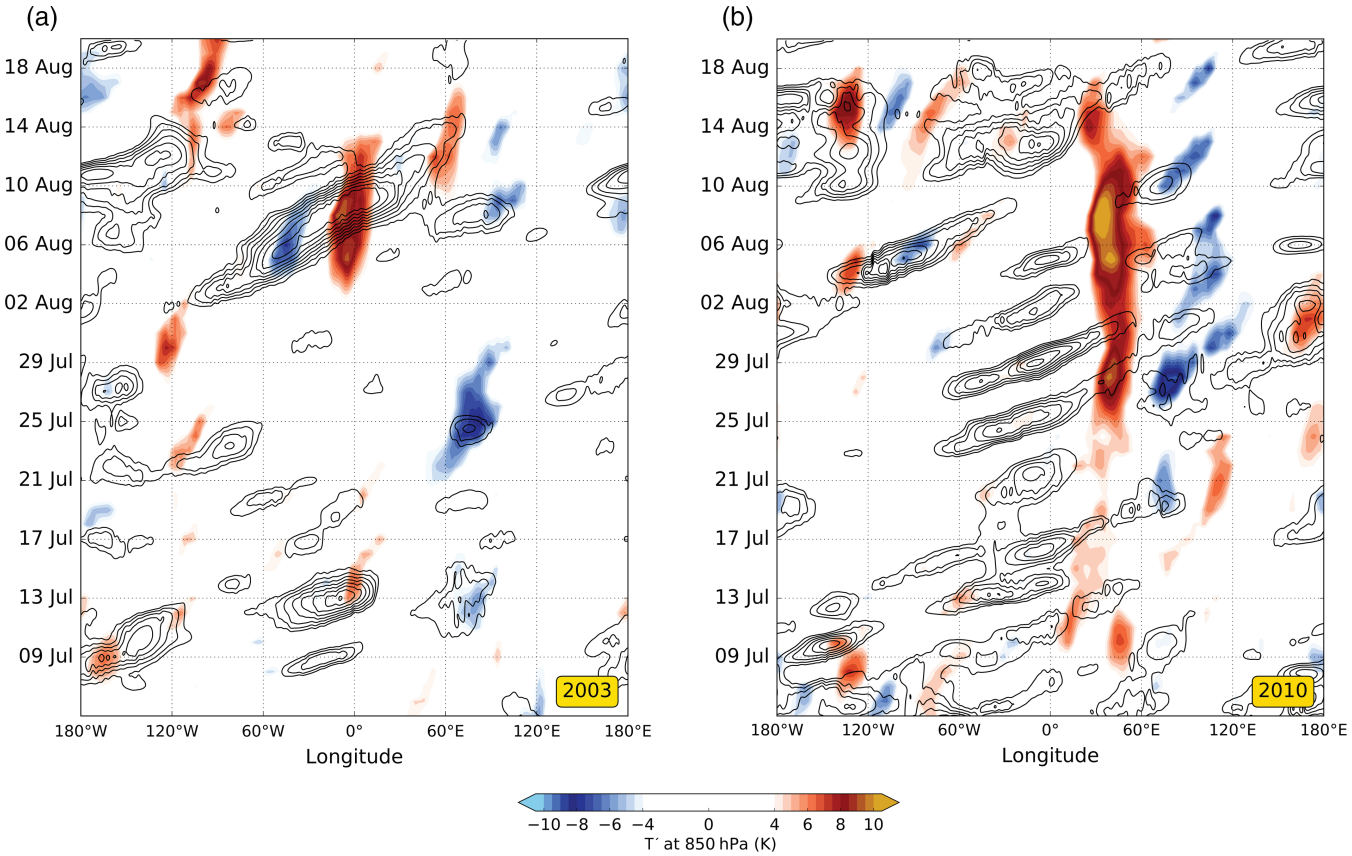


**Figure 10.** Hovmöller diagrams of temperature anomalies and RWP amplitudes for (a) the 2003 heat wave, and (b) the 2010 heat wave. The colour fill depicts 850 hPa $T'$ (K), averaged over 40-60°N in (a) and over 44–64°N in (b). The black contours depict the latitudinal average of 300 hPa $E$ (every 2 m s$^{-1}$, starting from 20 m s$^{-1}$). The latitudinal averaging for $E$ is explained in the text.

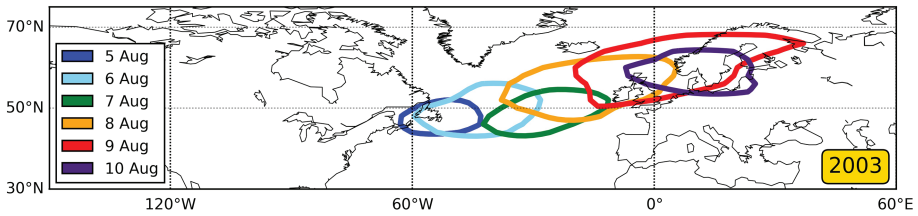


**Figure 11.** Location of the RWP highest amplitudes ($E = 35$ m s$^{-1}$) on consecutive days between 5 and 10 August during the 2003 heat wave. Each colour contour represents a different day.

The observed quasi-stationarity of strong southerlies to the west of Europe was associated with a strong ridge-building downstream over the affected areas. This ridge presumably played a major role in an initial northward advection of the background isotherms and later in favouring and sustaining clear skies and *in situ* warming by adiabatic compression in subsiding air masses (Black *et al.*, 2004; Bieli *et al.*, 2015). The persistent anticyclonic conditions and precipitation deficit of the preceding months led to reduced soil moisture and anomalously high SSTs, thus creating a susceptible environment and contributing to the rapid warming during the early stages of the event (3–5 August) and its eventual peak magnitude (Fischer *et al.*, 2007b; Hirschi *et al.*, 2011; Feudale and Shukla, 2011). The spatially varying impact of the aforementioned processes within the large-scale ridge and the sensitivity to the thermodynamic properties of the air masses prior to the arrival of the RWP suggest that severely affected areas should not necessarily be exactly collocated with areas of peak RWP amplitude (Figures 9(a) and 11).

Unlike the 2003 case, the 2010 heat wave is characterized by a continuous succession of strong RWPs over the North Atlantic and Europe (Figure 10(b)). At the same time there is a gradual build-up of anomalously warm temperatures in Western Russia. Figure 12(b) reveals that, at the longitudes where the RWPs started decaying (i.e. around 0–30°E ), they were always associated with a strong southerly wind component. The consecutive passages of RWPs and the variable strength of the embedded southerlies is associated with the western flank of an intermittent atmospheric block over Russia, as investigated in previous studies (Matsueda, 2011; Schneidereit *et al.*, 2012). In the latest phase of the event, the RWPs started to weaken (around 6 August), but southerlies – not clearly embedded in a larger-scale RWP – were maintained for a few more days. At this stage land–atmosphere feedbacks and the formation of deep and warm nocturnal residual layers effectively contributed in the intensification of the event (Lau and Kim, 2012; Miralles *et al.*, 2014). It was during this period (4–10 August), that the heat wave reached its maximum intensity (Figure 10(b)). Interestingly, this late period was also characterized by poor predictability, with several weather forecasting centres underestimating the severity of the event (Matsueda, 2011; Quandt *et al.*, 2017).

This analysis reveals that, although both heat waves were associated with strong RWPs, there were also some striking differences. For instance, in 2003, one strong RWP was coincident with the most extreme part of the heat wave. In contrast, in 2010, consecutive RWPs seemed to contribute to establishing the heat wave, while its phase of peak intensity was accompanied by rather weak RWP activity. This suggests that, depending on their characteristics (amplitude, structure, group velocity, phase velocity of embedded eddies, etc.) and the interplay with other physical processes, there may be various direct or indirect

mechanisms through which a RWP contributes to a heat wave or temperature extreme in general.

## 5. Summary and discussion

This study focused on the linkage between Rossby wave packets and temperature extremes in the Northern Hemisphere. We found that, in many regions of the midlatitudes, the presence of large-amplitude RWPs in the upper troposphere is associated with a considerably increased probability of lower-tropospheric temperature extremes. A significant inter-regional and seasonal variability in this correspondence was observed. Furthermore, it was found that in most regions the non-circumglobal RWP amplitudes are much better linked to temperature extremes than Fourier amplitudes quantifying circumglobal waviness. The advantage of identifying and following the evolution of RWPs was also revealed in two specific cases of recent extreme heat waves. Although the connection between RWP amplitude and temperature anomaly was not straightforward at every instance during the two episodes (suggesting more mechanisms at work), both heat waves were associated with conspicuous non-circumglobal RWP activity.

In the past, several studies used Fourier analysis of the upper-tropospheric meridional wind or geopotential height in order to link temperature extremes to amplified planetary waves in daily to monthly mean datasets (Petoukhov *et al.*, 2013; Coumou *et al.*, 2014; Screen and Simmonds, 2014; Kornhuber *et al.*, 2017). As Hoskins and Woollings (2015) pointed out, even regionally confined RWPs inevitably possess power in a range of zonal wavenumbers when subjected to Fourier analysis. However, this by no means implies the existence of circumglobal waves. Furthermore, temporal and zonal averaging in the aforementioned studies obscures essential information on the synoptic evolution and may lead to a misleading impression about the characteristics of the extremes and the role of the upper-tropospheric circulation. For example, time filtering (e.g. 15-day running mean or monthly mean) may give equal weight to a strong but short-lived anomaly and a weak but persistent anomaly. In addition, such a time filtering in the case of the 2010 heat wave, for example, would conceal the successive eastward propagation of longitudinally confined maxima in upper-tropospheric wave amplitude (RWPs). Similarly, zonal averaging may give equal weight to strong but regionally restricted and weak but hemispherically extended anomalies. Peaks in the zonally averaged zonal wind (in particular) cannot be safely interpreted or attributed to specific flow regimes. We believe that these distinctions are essential in the context of weather extremes. Indeed, the two specific cases which we investigated showed that heat waves of similar strength can be associated with highly distinctive daily evolutions of the upper-tropospheric circulation. It appears necessary to account for such differences in order to unravel the relevant mechanisms and improve our understanding of weather extremes.

As a step forward, in the present study we used the concept of RWPs, the presence of which suggests that waviness in the upper troposphere is typically not stretched out circumglobally, but organized in eastward-propagating patches of limited spatial extent. Investigation of these structures is important because they embody and possibly moderate the synoptic-scale systems (cyclones, blocks, etc.) that are associated with regional flow patterns and physical processes within those patterns that favour the occurrence of temperature extremes (Kyselỳ, 2008; Pfahl and Wernli, 2012; Bieli *et al.*, 2015; Chang *et al.*, 2016). Consequently, using the RWP amplitude as an upper-tropospheric waviness metric gave us a more direct link to lower-tropospheric temperature extremes. In a similar vein, Röthlisberger *et al.* (2016) employed a regional-scale jet waviness diagnostic using the geometry of the 2 pvu contour on an upper-tropospheric isentrope and showed that it has a clearer link to weather extremes than a hemispheric jet waviness metric.

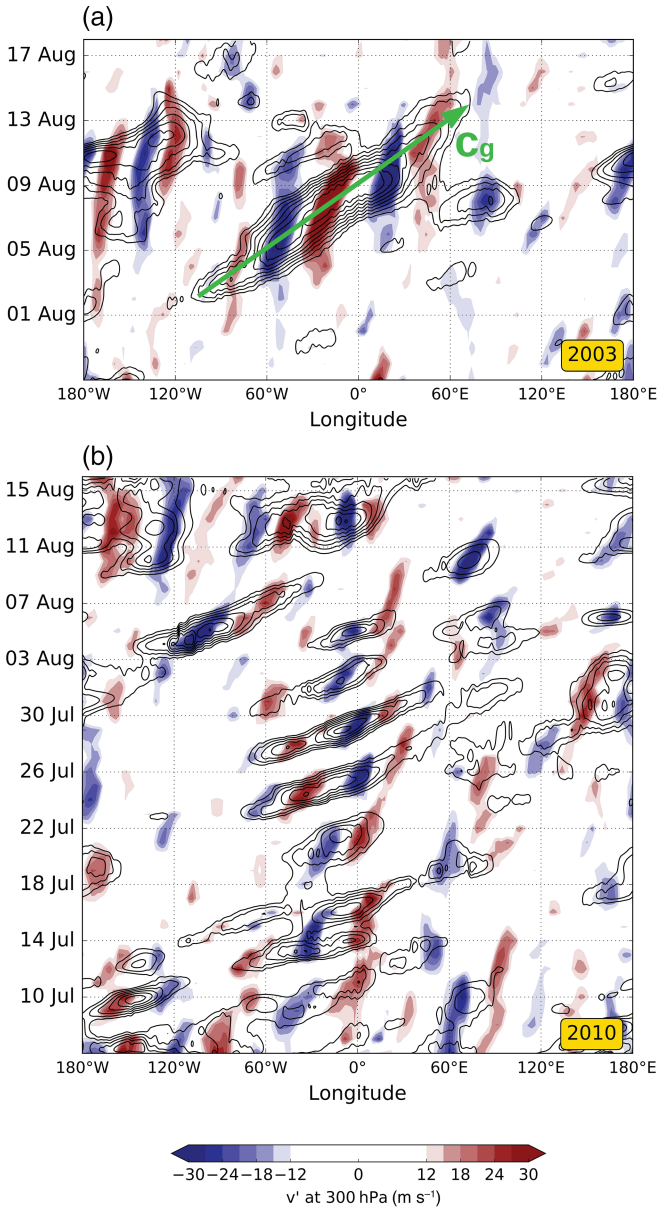


**Figure 12.** Hovmöller diagrams illustrating the upper-tropospheric flow for (a) the 2003 heat wave, and (b) the 2010 heat wave. The black contours depict the latitudinal average of 300 hPa $E$ (every 2 m s$^{-1}$, starting from 20 m s$^{-1}$). The colour fill depicts 300 hPa $v'$. The green arrow in (a) indicates the group velocity ($\mathbf{c}_g$) of the RWP.

The observed variability in the connection between RWP amplitude and synoptic-scale temperature extremes revealed noticeable differences between the summer and winter seasons (Figures 4 and 6). Apart from some regions to the north of UK and in the Gulf of Alaska, most parts of the Northern Hemisphere midlatitudes had a reduced $\mathcal{P}$ during winter (fewer temperature extremes occurring in the top 20% $E$ than in summer). This decrease was more pronounced in areas of North America, North Atlantic, Europe and Central Asia. Given our analysis, this summer–winter difference can occur because during winter there are more mechanisms that lead to $|T'|$ extremes in days without a strong RWP amplitude (involving e.g. mesoscale vorticity features of wave-breaking, strong temperature advection from zonal winds or enhanced orographic effects) and/or because some winter synoptic systems are associated with enhanced upper-troposphere waviness but no equivalent anomalies in the lower-troposphere temperatures. Both of these cases will lead to reduced $\mathcal{P}$. An in-depth investigation of the inherent dynamic and thermodynamic characteristics of the two seasons would be required to fully explain the seasonal variability of $\mathcal{P}$. One thing to note is the extended variability in both $E$ and 2 m/850 hPa $|T'|$ during winter, as indicated by the respective 90th percentile

climatologies (Figure B1). In addition, persistent winter-time inversions in the lower-tropospheric temperature profile caused by compressional warming in subsiding air within high pressure systems or by surface radiative cooling (particularly effective in dry continental regions with long nights) lead to a stable lower troposphere and the gradual formation of compact air masses with characteristic temperature and relative humidity (acquired by the underlying surface properties). These air masses are then advected away by the strong synoptic systems of winter, temporarily maintaining their temperature (unperturbed by strong surface fluxes and convection; a characteristic of summer) and potentially passing over a region with different characteristics, thus causing large temperature anomalies or instability followed by organized precipitation. Such situations may lead to one of the two cases reducing $\mathcal{P}$ as described earlier.

One limitation in our work arises when using the RWP amplitude as the only metric to quantify the linkage between upper-tropospheric waviness and lower-tropospheric temperature extremes. For instance, this linkage may become even stronger when taking into account the phase velocities of the embedded troughs and ridges and the initial thermodynamic properties of the air masses underneath. When the troughs and ridges propagate slowly in the zonal direction, they favour and maintain processes that can intensify the lower-tropospheric temperature anomalies and lead to temperature extremes. We showed that this was true for the two heat waves considered, but it is conceivable that this is not always satisfied. In fact, the intermittent heat wave over Europe in August–September 2016 may be such a case, where a large phase velocity prevented a long-lasting heat wave (Zschenderlein *et al.*, 2018; personal communication). In addition, when a lower-tropospheric air mass is already warmer (colder) than average, an incoming RWP with only moderate amplitude may still be enough to favour a hot (cold) extreme. Another limitation, which is left for future work, comes from the fact that our two-dimensional RWP amplitude field detects all synoptic systems that are associated with a strong meridional wind component in the upper troposphere, without distinguishing between systems that favour explicitly hot or cold temperature extremes (also Appendix A). Regarding the two cases of the 2003 and 2010 heat waves, a complete investigation of these events would require an analysis of many factors acting across multiple scales. Since our analysis aimed at specific considerations regarding the role of RWPs, the important contribution of other physical mechanisms (related e.g. to radiative transfer, SST, subsidence, soil moisture, etc.) was only briefly mentioned.

Based on the results presented in this study, we conclude that RWPs are closely connected with the occurrence of lower-tropospheric temperature extremes. This calls for enhanced efforts to better understand the mechanisms that lead to the amplification of RWPs and determine their velocity and track, with potential benefits both in the context of weather forecasting and for climate change research. Dedicated studies are also required to tackle questions raised by the intriguing inter-regional and seasonal variability which was found in our analyses. Complementing such investigations with studies on the role of other relevant physical processes mentioned in the text would then pave the way to a better understanding of the predictability of temperature extremes and their characteristics in a changing climate.

**Acknowledgements**

We thank the ECMWF for providing access to the data used in this study. We are grateful to the reviewers for their remarks, as well as to Gabriel Wolf and Federico Grazzini for insightful discussions. The research leading to these results has been done within the Transregional Collaborative Research Center SFB/TRR 165 'Waves to Weather' funded by the German Science Foundation (DFG).

## Appendix A: Sensitivity of the results

In our envelope calculation methodology, we imposed a filter limiting the wavelength to the range 2000–10 000 km. The corresponding results and implications turned out to be insensitive to small variations in the limits of this range of wavelengths. In addition, the results in Figures 3–6 where we used only every third date of the 1979–2015 summers do not change substantially by the inclusion/exclusion of more dates. Finally, when repeating the analyses of Figures 4 and 6 for the top 5% hot or cold temperature extremes instead of the top 10% of $|T'|$, it is revealed that in many regions the linkage with RWP amplitude is particularly good for temperature extremes of one sign and less so for the opposite one. A dedicated study would be needed to explore this observation further.

Our analysis does not assume or imply a strict collocation and coincidence of strong upper-tropospheric RWP amplitude and lower-tropospheric (850 hPa, 2 m) temperature extremes. The imperfect correlation we found is in part caused by spatio-temporal offsets (lags) between these fields, which are expected to occur in a case-sensitive manner. In order to avoid fragile assumptions about typical magnitudes of these offsets, in the analyses of Figures 3, 4 and 6 we tried to minimize such effects by looking at daily mean fields, averaged over the same $20^\circ \times 20^\circ$ area. Regarding the Fourier analysis, we tested using zonal wavenumber ranges which were narrower than 1–15 and more restricted to the typical wavelengths of transient Rossby waves (e.g. wavenumbers 5–9), but the loss of information resulted in even lower correlations with the temperature extremes.

The values in Figures 4–6 quantify the percentage of $|T'|$ extremes (defined as $|T'| >$ 90th percentile) in the highest two $E$-bins. We repeated the analysis using other metrics for the connection between 300 hPa RWP amplitude and 850 hPa temperature extremes, such as

(i) the Spearman's rank correlation coefficient (Figures 3(a) and (c)),
(ii) the difference between the highest and lowest two $E$-bin averages, and
(iii) the linear fit slope of the data points in Figures 3(b) and (d).

In all cases the results and main conclusions remained qualitatively and quantitatively similar.

Regarding the Hovmöller diagrams (Figure 10), we tested several latitude bands for the latitudinal averaging (continuous or intermittent) and again found no substantial changes in our main results. In addition, the 2 m temperature gives similar results to the 850 hPa temperature, no matter whether we averaged over all grid points or over land grid points only.

Finally, we repeated our analysis with RWPs diagnosed from the meridional wind at 200 hPa and 500 hPa, instead of 300 hPa, which was chosen in this study as an indicative level for the study of Rossby waves. The magnitudes of meridional wind anomalies are changing, and the detected RWP amplitude fields are not perfectly collocated at these three levels. As expected, the correlations with $|T'|$ at 850 hPa are slightly increased (decreased) for RWP amplitude calculated at 500 hPa (200 hPa). For example, the equivalent analysis of Figure 3(a) gave Spearman's rank correlation coefficients of 0.52 and 0.39 for 500 and 200 hPa, respectively.

## Appendix B: Maps of the 90th percentile of anomalies in temperature, RWP amplitude, and Fourier amplitude

As a complement to the analyses in section 3, Figure B1 shows maps of the Northern Hemisphere summer and winter 90th percentile of daily mean temperature anomalies from climatology at 850 hPa and 2 m for every $20^\circ \times 20^\circ$ region. These maps highlight the areas where temperature deviations tend to be large. Overall, daily mean temperature anomalies are higher in winter than in summer, and there is a poleward increase for both seasons. The values are generally lower over the oceans

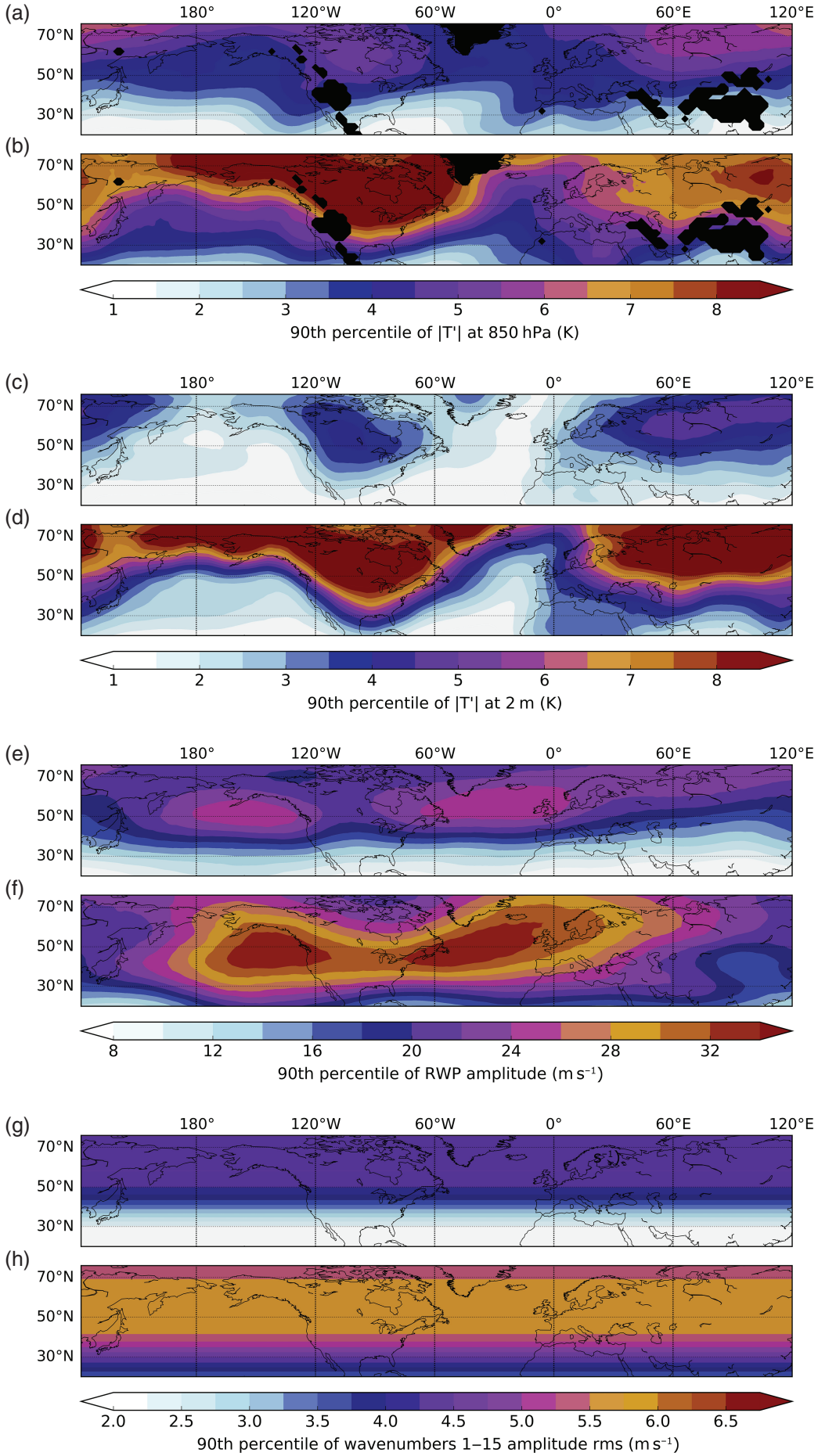


**Figure B1.** Summer (JJA) 90th percentile of daily mean (a) $|T'|$ at 850 hPa (K), (c) $|T'|$ at 2 m (K) (e) RWP amplitude (m s$^{-1}$) and (g) root mean square of the Fourier transform zonal wavenumber 1–15 amplitudes of the 300 hPa $v'$. (b), (d), (f), (h) show winter (DJF) 90th percentile maps for the respective quantities. The percentiles in (a)–(f) are calculated for the spatial averages of the 20° ×20° regions centred on every grid point. In (g) and (h), the values shown are $v'$ meridionally averaged in the 20° zonal band centred over every grid point. In (a) and (b), grid points with a mean surface pressure below 850 hPa are shown in black.

than over the continents, which is a well-known feature related to the difference between maritime and continental climates (Hartmann, 2015).

Figures B1(e) and (f) show maps of the 90th percentile of daily mean RWP amplitude anomalies. As with temperature, daily mean RWP amplitude anomalies are larger in winter than in summer, and generally they tend to be maximum over the storm track regions. As expected, the winter–summer difference is also evident in the corresponding maps of the root mean square of the Fourier transform zonal wavenumber 1–15 amplitudes of the 300 hPa $v'$ (Figures B1(g) and (h)). By construction, the latter show no variation in longitude.

## References


Anthes RA, Kuo YH, Baumhefner DP, Errico RM, Bettge TW. 1985. Predictability of mesoscale atmospheric motions. *Adv. Geophys.* **28**: 159–202. https://doi.org/10.1016/S0065-2687(08)60188-0.

Barnes EA, Screen JA. 2015. The impact of Arctic warming on the midlatitude jet stream: Can it? Has it? Will it?. *WIREs Clim. Change* **6**: 277–286. https://doi.org/10.1002/wcc.337.

Bieli M, Pfahl S, Wernli H. 2015. A Lagrangian investigation of hot and cold temperature extremes in Europe. *Q. J. R. Meteorol. Soc.* **141**: 98–108. https://doi.org/10.1002/qj.2339.

Black E, Blackburn M, Harrison G, Hoskins BJ, Methven J. 2004. Factors contributing to the summer 2003 European heatwave. *Weather* **59**: 217–223. https://doi.org/10.1256/wea.74.04.

Butler AH, Thompson DW, Heikes R. 2010. The steady-state atmospheric circulation response to climate change-like thermal forcings in a simple general circulation model. *J. Clim.* **23**: 3474–3496. https://doi.org/10.1175/2010JCLI3228.1.

Chang EK. 1993. Downstream development of baroclinic waves as inferred from regression analysis. *J. Atmos. Sci.* **50**: 2038–2053. https://doi.org/10.1175/1520-0469(1993)050<2038:ddobwa>2.0.CO;2.

Chang EK. 2001. The structure of baroclinic wave packets. *J. Atmos. Sci.* **58**: 1694–1713. https://doi.org/10.1175/1520-0469(2001)058<1694:tsobwp>2.0.CO;2.

Chang EK, Ma CG, Zheng C, Yau AM. 2016. Observed and projected decrease in Northern Hemisphere extratropical cyclone activity in summer and its impacts on maximum temperature. *Geophys. Res. Lett.* **43**: 2200–2208. https://doi.org/10.1002/2016GL068172.

Coumou D, Petoukhov V, Rahmstorf S, Petri S, Schellnhuber HJ. 2014. Quasi-resonant circulation regimes and hemispheric synchronization of extreme weather in boreal summer. *Proc. Natl. Acad. Sci. U.S.A.* **111**: 12331–12336. https://doi.org/10.1073/pnas.1412797111.

Davies HC. 2015. Weather chains during the 2013/2014 winter and their significance for seasonal prediction. *Nat. Geosci.* **8**: 833–837. https://doi.org/10.1038/ngeo2561.

Dee DP, Uppala SM, Simmons AJ, Berrisford P, Poli P, Kobayashi S, Andrae U, Balmaseda MA, Balsamo G, Bauer P, Bechtold P, Beljaars ACM, van de Berg L, Bidlot J, Bormann N, Delsol C, Dragani R, Fuentes M, Geer AJ, Haimberger L, Healy SB, Hersbach H, Hólm EV, Isaksen L, Kållberg P, Köhler M, Matricardi M, McNally AP, Monge-Sanz BM, Morcrette J-J, Park B-K, Peubey C, de Rosnay P, Tavolato C, Thépaut J-N, Vitart F. 2011. The ERA-Interim reanalysis: Configuration and performance of the data assimilation system. *Q. J. R. Meteorol. Soc.* **137**: 553–597. https://doi.org/10.1002/qj.828.

Esler J, Haynes P. 1999. Mechanisms for wave packet formation and maintenance in a quasi-geostrophic two-layer model. *J. Atmos. Sci.* **56**: 2457–2490. https://doi.org/10.1175/1520-0469(0)056<2457:mfwpfa>2.0.CO;2.

Feudale L, Shukla J. 2011. Influence of sea surface temperature on the European heat wave of 2003 summer. Part I: an observational study. *Clim. Dyn.* **36**: 1691–1703. https:// doi.org/10.1007/s00382-010-0788-0.

Fink AH, Brücher T, Krüger A, Leckebusch GC, Pinto JG, Ulbrich U. 2004. The 2003 European summer heatwaves and drought – synoptic diagnosis and impacts. *Weather* **59**: 209–216. https://doi.org/10.1256/wea.73.04.

Fischer EM, Seneviratne SI, Lüthi D, Schär C. 2007a. Contribution of land–atmosphere coupling to recent European summer heat waves. *Geophys. Res. Lett.* **34**: L06707. https://doi.org/10.1029/2006GL029068.

Fischer EM, Seneviratne SI, Vidale P, Lüthi D, Schär C. 2007b. Soil moisture–atmosphere interactions during the 2003 European summer heat wave. *J. Clim.* **20**: 5081–5099. https://doi.org/10.1175/JCLI4288.1.

Garca-Herrera R, Daz J, Trigo R, Luterbacher J, Fischer EM. 2010. A review of the European summer heat wave of 2003. *Crit. Rev. Environ. Sci. Technol.* **40**: 267–306. https://doi.org/10.1080/10643380802238137.

Garfinkel CI, Harnik N. 2017. The non-Gaussianity and spatial asymmetry of temperature extremes relative to the storm track: The role of horizontal advection. *J. Clim.* **30**: 445–464. https://doi.org/10.1175/JCLI-D-15-0806.1.

Glatt I, Dörnbrack A, Jones S, Keller J, Martius O, Müller A, Peters DH, Wirth V. 2011. Utility of Hovmöller diagrams to diagnose Rossby wave trains. *Tellus A* **63**: 991–1006. https://doi.org/10.1111/j.1600-0870.2011.00541.x.

Grazzini F, Vitart F. 2015. Atmospheric predictability and Rossby wave packets. *Q. J. R. Meteorol. Soc.* **141**: 2793–2802. https://doi.org/10.1002/qj.2564.

Harris FJ. 1978. On the use of windows for harmonic analysis with the discrete Fourier transform. *Proc. IEEE* **66**: 51–83.

Hartmann DL. 2015. *Global Physical Climatology*. Elsevier: Amsterdam, Netherlands.

Harvey B, Shaffrey L, Woollings T. 2014. Equator-to-pole temperature differences and the extratropical storm track responses of the CMIP5 climate models. *Clim. Dyn.* **43**: 1171–1182. https://doi.org/10.1007/s00382-013-1883-9.

Hauser M, Orth R, Seneviratne SI. 2016. Role of soil moisture versus recent climate change for the 2010 heat wave in western Russia. *Geophys. Res. Lett.* **43**: 2819–2826. https://doi.org/10.1002/2016GL068036.

Hirschi M, Seneviratne SI, Alexandrov V, Boberg F, Boroneant C, Christensen OB, Formayer H, Orlowsky B, Stepanek P. 2011. Observational evidence for soil-moisture impact on hot extremes in southeastern Europe. *Nat. Geosci.* **4**: 17–21. https://doi.org/10.1038/ngeo1032.

Horton RM, Mankin JS, Lesk C, Coffel E, Raymond C. 2016. A review of recent advances in research on extreme heat events. *Curr. Clim. Change Rep.* **2**: 242–259. https://doi.org/10.1007/s40641-016-0042-x.

Hoskins BJ, Woollings T. 2015. Persistent extratropical regimes and climate extremes. *Curr. Clim. Change Rep.* **1**: 115–124. https://doi.org/10.1007/s40641-015-0020-8.

Kornhuber K, Petoukhov V, Petri S, Rahmstorf S, Coumou D. 2017. Evidence for wave resonance as a key mechanism for generating high-amplitude quasi-stationary waves in boreal summer. *Clim. Dyn.* **49**: 1961–1979. https://doi.org/10.1007/s00382-016-3399-6.

Kyselỳ J. 2008. Influence of the persistence of circulation patterns on warm and cold temperature anomalies in Europe: Analysis over the 20th century. *Global Planet. Change* **62**: 147–163. https://doi.org/10.1016/j.gloplacha.2008.01.003.

Lackmann G. 2011. *Midlatitude Synoptic Meteorology*. American Meteorological Society: Boston.

Lau NC, Nath MJ. 2014. Model simulation and projection of European heat waves in present-day and future climates. *J. Clim.* **27**: 3713–3730. https://doi.org/10.1175/JCLI-D-13-00284.1.

Lau WK, Kim KM. 2012. The 2010 Pakistan flood and Russian heat wave: Teleconnection of hydrometeorological extremes. *J. Hydrometeorol.* **13**: 392–403. https://doi.org/10.1175/JHM-D-11-016.1.

Lee S, Held IM. 1993. Baroclinic wave packets in models and observations. *J. Atmos. Sci.* **50**: 1413–1428. https://doi.org/10.1175/1520-0469(1993)050<1413:bwpima>2.0.CO;2.

Lyon B, Dole RM. 1995. A diagnostic comparison of the 1980 and 1988 US summer heat-wave droughts. *J. Clim.* **8**: 1658–1675. https://doi.org/10.1175/1520-0442(1995)008<1658:adcota>2.0.CO;2.

Martius O, Schwierz C, Davies HC. 2008. Far-upstream precursors of heavy precipitation events on the Alpine south-side. *Q. J. R. Meteorol. Soc.* **134**: 417–428. https://doi.org/10.1002/qj.229.

Matsueda M. 2011. Predictability of Euro-Russian blocking in summer of 2010. *Geophys. Res. Lett.* **38**: L06801. https://doi.org/10.1029/2010GL046557.

Meehl GA, Tebaldi C. 2004. More intense, more frequent, and longer lasting heat waves in the 21st century. *Science* **305**: 994–997. https://doi.org/10.1126/science.1098704.

Miralles DG, Teuling AJ, Van Heerwaarden CC, de Arellano JVG. 2014. Mega-heatwave temperatures due to combined soil desiccation and atmospheric heat accumulation. *Nat. Geosci.* **7**: 345–349. https://doi.org/10.1038/ngeo2141.

Otto FE, Massey N, Oldenborgh G, Jones R, Allen M. 2012. Reconciling two approaches to attribution of the 2010 Russian heat wave. *Geophys. Res. Lett.* **39**: L04702. https://doi.org/10.1029/2011GL050422.

Petoukhov V, Rahmstorf S, Petri S, Schellnhuber HJ. 2013. Quasi-resonant amplification of planetary waves and recent Northern Hemisphere weather extremes. *Proc. Natl. Acad. Sci. U.S.A.* **110**: 5336–5341. https://doi.org/10.1073/pnas.1222000110.

Pfahl S, Wernli H. 2012. Quantifying the relevance of atmospheric blocking for co-located temperature extremes in the Northern Hemisphere on (sub-)daily time scales. *Geophys. Res. Lett.* **39**: L12807. https://doi.org/10.1029/2012GL052261.

Quandt LA, Keller JH, Martius O, Jones SC. 2017. Forecast variability of the blocking system over Russia in summer 2010 and its impact on surface conditions. *Weather and Forecasting* **32**: 61–82. https://doi.org/10.1175/WAF-D-16-0065.1.

Quinting JF, Jones SC. 2016. On the impact of tropical cyclones on Rossby wave packets: A climatological perspective. *Mon. Weather Rev.* **144**: 2021–2048. https://doi.org/10.1175/MWR-D-14-00298.1.

Rahmstorf S, Coumou D. 2011. Increase of extreme events in a warming world. *Proc. Natl. Acad. Sci. U.S.A.* **108**: 17905–17909. https://doi.org/10.1073/pnas.1101766108.

Röthlisberger M, Pfahl S, Martius O. 2016. Regional-scale jet waviness modulates the occurrence of midlatitude weather extremes. *Geophys. Res. Lett.* **43**: 10989–10997. https://doi.org/10.1002/2016GL070944.

Russo S, Dosio A, Graversen RG, Sillmann J, Carrao H, Dunbar MB, Singleton A, Montagna P, Barbola P, Vogt JV. 2014. Magnitude of extreme heat waves in present climate and their projection in a warming world. *J. Geophys. Res. Atmos.* **119**: 12500–12512. https://doi.org/10.1002/2014JD022098.

Russo S, Sillmann J, Fischer EM. 2015. Top ten European heatwaves since 1950 and their occurrence in the coming decades. *Environ. Res. Lett.* **10**: 124003. https://doi.org/10.1088/1748-9326/10/12/124003.

Schär C, Vidale PL, Lüthi D, Frei C, Häberli C, Liniger MA, Appenzeller C. 2004. The role of increasing temperature variability in European summer heatwaves. *Nature* **427**: 332–336. https://doi.org/10.1038/nature02300.

Schneider T, Bischoff T, Potka H. 2015. Physics of changes in synoptic midlatitude temperature variability. *J. Clim.* **28**: 2312–2331. https://doi.org/10.1175/JCLI-D-14-00632.1.

Schneidereit A, Schubert S, Vargin P, Lunkeit F, Zhu X, Peters DH, Fraedrich K. 2012. Large-scale flow and the long-lasting blocking high over Russia: Summer 2010. *Mon. Weather Rev.* **140**: 2967–2981. https://doi.org/10.1175/MWR-D-11-00249.1.

Schubert S, Wang H, Suarez M. 2011. Warm season subseasonal variability and climate extremes in the Northern Hemisphere: The role of stationary Rossby waves. *J. Clim.* **24**: 4773–4792. https://doi.org/10.1175/JCLI-D-10-05035.1.

Screen JA, Simmonds I. 2014. Amplified mid-latitude planetary waves favour particular regional weather extremes. *Nat. Clim. Change* **4**: 704–709. https://doi.org/10.1038/nclimate2271.

Shepherd TG. 2014. Atmospheric circulation as a source of uncertainty in climate change projections. *Nat. Geosci.* **7**: 703–708. https://doi.org/10.1038/ngeo2253.

Simmons AJ, Hoskins BJ. 1979. The downstream and upstream development of unstable baroclinic waves. *J. Atmos. Sci.* **36**: 1239–1254. https://doi.org/10.1175/1520-0469(1979)036<1239:tdaudo>2.0.CO;2.

Souders MB, Colle BA, Chang EK. 2014. The climatology and characteristics of Rossby wave packets using a feature-based tracking technique. *Mon. Weather Rev.* **142**: 3528–3548. https://doi.org/10.1175/MWR-D-13-00371.1.

Stocker TF, Qin D, Plattner G-K, Tignor M, Allen SK, Boschung J, Nauels A, Xia Y, Bex V, Midgley PM (eds). 2014. *Climate Change 2013: The Physical Science Basis: Working Group I Contribution to the Fifth Assessment Report of the Intergovernmental Panel on Climate Change*. Cambridge University Press: Cambridge, UK and New York, NY.

Sun L, Chen G, Lu J. 2013. Sensitivities and mechanisms of the zonal mean atmospheric circulation response to tropical warming. *J. Atmos. Sci.* **70**: 2487–2504. https://doi.org/10.1175/JAS-D-12-0298.1.

Teubler F, Riemer M. 2016. Dynamics of Rossby wave packets in a quantitative potential vorticity-potential temperature framework. *J. Atmos. Sci.* **73**: 1063–1081. https://doi.org/10.1175/JAS-D-15-0162.1.

Wirth V, Eichhorn J. 2014. Long-lived Rossby wave trains as precursors to strong winter cyclones over Europe. *Q. J. R. Meteorol. Soc.* **140**: 729–737. https://doi.org/10.1002/qj.2191.

Wolf G, Wirth V. 2015. Implications of the semigeostrophic nature of Rossby waves for Rossby wave packet detection. *Mon. Weather Rev.* **143**: 26–38. https://doi.org/10.1175/MWR-D-14-00120.1.

Zimin AV, Szunyogh I, Patil D, Hunt BR, Ott E. 2003. Extracting envelopes of Rossby wave packets. *Mon. Weather Rev.* **131**: 1011–1017. https://doi.org/10.1175/1520-0493(2003)131<1011:eeorwp>2.0.CO;2.